Journal of Solid State Chemistry **154,** 286–295 (2000)
doi:10.1006/jssc.2000.8851, available online at http://www.idealibrary.com on IDEAL®

Structural, Electronic, and Magnetic Properties of Ternary Rare-Earth Metal Borocarbides $R_5B_2C_5$ (R = Y, Ce–Tm) Containing BC_2 "Molecules"

Emmanuelle Bidaud and Kurt Hiebl[1]

Institut für Physikalische Chemie, Universität Wien, Währingerstrasse 42, A-1090 Wien, Austria

Rolf-Dieter Hoffmann and Rainer Pöttgen[1]

Institut für Chemie, Ludwig-Maximilians-Universität München Butenandtstrasse 5-13, D-81377 München, Germany

and

Christophe Jardin, Josef Bauer, Régis Gautier,[2] Patrick Gougeon, Jean-Yves Saillard, and Jean-François Halet[1,3]

Laboratoire de Chimie du Solide et Inorganique Moléculaire, UMR 6511 CNRS- Université de Rennes 1, Institut de Chimie de Rennes, F-35042 Rennes Cedex, France

Received December 30, 1999; in revised form May 12, 2000; accepted May 20, 2000

The borocarbides $R_5B_2C_5$ (R = Y, Ce–Tm) were prepared by arc melting from the pure rare-earth metals, boron and carbon. The structural arrangement of these compounds, which crystallize in the tetragonal space group *P4/ncc*, consists of a three-dimensional framework of rare-earth atoms resulting from the stacking of slightly corrugated two-dimensional squares, which lead to the formation of octahedral holes and distorted bicapped square antiprismatic cavities filled with isolated carbon atoms and C–B–C chains, respectively. In contrast to the heavy rare-earth metal (Gd–Tm)-containing compounds which melt congruently, those with the early rare-earth elements (Ce–Sm) are formed peritectically. The electronic structure and chemical bonding of $Sm_5B_2C_5$ and $Gd_5B_2C_5$ are analyzed using extended Hückel tight-binding and density-functional theory calculations. Results reveal a rather strong covalency between the metallic matrix and the BC_2 groups and the isolated carbon atoms, respectively, similar to what is generally computed in related rare-earth metal borocarbides. Magnetic susceptibility measurements indicate that all samples, which were investigated, undergo ferromagnetic transitions in the temperature region below T = 130 K. The heavy rare-earth metal (Tb–Tm) borocarbides exhibit a magnetic behavior typical of narrow-domain-wall ferromagnets. Both the Curie temperatures, T_C, as well as the paramagnetic Curie temperatures, Θ_P, scale approximately with the de Gennes factor. Hence the indirect exchange interaction via conduction electrons (RKKY-interacting) is the dominating force of the R–R coupling mechanism. © 2000 Academic press

Key Words: **rare-earth metal borocarbide; structural chemistry; electronic structure; EHTB calculations; DFT calculations; magnetism.**

INTRODUCTION

Ternary phases resulting from the combination of boron and carbon with rare-earth metals (R) receive nowadays increasing attention because of their structural, mechanical, electrical, and magnetic properties (1–4). In these compounds, boron and carbon atoms generally form either two-dimensional (2D) networks, which alternate with 2D sheets of metal atoms, or one-dimensional (1D) carbon-branched zigzag boron chains running into channels built by the metal atoms, or finite pseudomolecules of various sizes trapped into holes built by the metallic matrix. Such a broad diversity of original topologies, especially with respect to the bonding within the nonmetal frameworks, have rendered these compounds of interest for the theoretical chemists, who have rather quite intensively studied their electronic properties (1). In contrast, little is known about the magnetic behavior of these compounds (2–4). This work reports the synthesis, electronic structure, and magnetic properties

[1]E-mail: kurt.hiebl@univie.ac.at, rapch@cup.uni-muenchen.de, and jean-francois.halet@univ-rennes1.fr.

[2]Present address: Laboratoire de Physicochimie, UPRES 1795, Ecole Nationale Supérieure de Chimie de Rennes, F-35700 Rennes, France.

[3]To whom correspondence should be addressed.

0022-4596/00 $35.00

of a new family of ternary rare-earth metal boron carbides of composition $R_5B_2C_5$ (R = Y, Ce–Tm).

EXPERIMENTAL

Preparation. Mixtures of powders of the commercially available elements of high purity (99.99% rare-earth ingots, Rhône Poulenc, AZ; 99.8% crystalline boron powder, H. C. Starck, Germany; 99.98% graphite powder, Carbone-Lorraine, France) were compacted in stainless steel dies without the use of binders or lubricants. The pellets were arc-melted under purified (Ti-gettered) argon with a thoriated tungsten electrode. The buttons were turned over and remelted three times to ensure homogeneity. Weight losses were checked to be within 1% of the original mass (1 g). The molten pellets were broken into two parts. One part was studied in as-cast condition, the second part was annealed at 1270 K in silica tubes under primary vacuum for 10 days and subsequently quenched in cold water. To avoid any contamination, the samples were wrapped in molybdenum foil. The pellets had to be kept in sealed quartz tubes under primary vacuum to prevent hydrolysis of the samples.

X-ray analysis. X-ray powder photographs were obtained from all samples using a Debye-Scherrer camera ($\varnothing$ = 114.6 mm) with vanadium filtered Cr$K\alpha$ radiation. Being extremely moisture sensitive the powdered samples were enclosed with cyclohexane in 0.3-mm Lindemann capillaries. Small crystals suitable for X-ray analysis were isolated by mechanical fragmentation of the samples. Intensity data for the crystal structure analysis of $Gd_5B_2C_5$ were collected on an Enraf-Nonius CAD-4 diffractometer equipped with graphite-monochromatized Mo$K\alpha$ radiation. The data for the $Sm_5B_2C_5$ crystal were collected by use of a Stoe image plate system equipped with graphite-monochromatized Mo$K\alpha$ radiation. Preliminary results on the structure refinements of $Sm_5B_2C_5$ and $Gd_5B_2C_5$ indicate that they crystallize in the tetragonal space $P4/ncc$–D_{4h}^8 (No. 130) group with the lattice parameters a = 8.331(1) and 8.2455(3) Å and c = 10.926(7) and 10.8550(6) Å for $Sm_5B_2C_5$ and $Gd_5B_2C_5$, respectively. The positional parameters are as follows: Sm(1) (16g) 0.03955(9), 0.84440(8), 0.39757(6); Sm(2) (4c) 1/4, 1/4, 0.3583(1); B (8f) 0.091(2), 0.591(2), 1/4; C(1) (16g) 0.051(2), 0.649(1), 0.126(2); C(2) (4c) 1/4, 1/4, 0.600(2) for $Sm_5B_2C_5$ ($R1$ = 0.098, w$R2$ = 0.369 for 2320 reflections), and Gd(1) (16g) 0.0390(1), 0.8446(1), 0.3985(1); Gd(2) (4c) 1/4, 1/4, 0.3581(1); B (8f) 0.091(1), 0.5914(1), 3/4; C(1) (16g) 0.0517(1), 0.6471(1), 0.1257(9); C(2) (4c) 1/4, 1/4, 0.599(2) for $Gd_5B_2C_5$ ($R1$ = 0.0558, w$R2$ = 0.1328 for 1143 reflections with $I > 2\,\sigma(I)$). Both the $Sm_5B_2C_5$ and the $Gd_5B_2C_5$ structures show a strong tendency for twinning with a mechanism similar to that recently observed for Sc_3C_4 (5). These structures have NaCl-related layers (those with the Sm_6C octahedra) which are bridged via the BC_2 units. These NaCl layers and thus the chains of edge-sharing octahedra emphasized in Fig. 1 can be rotated around the c axis by about 45°, leading to twinning. The detailed structural investigation will be published in a forthcoming paper.

Magnetic measurements. Magnetic susceptibilities were measured using a Faraday pendulum magnetometer SUS 10 above liquid nitrogen (temperature up to 500 K) and in external fields varying from 0.1 to 1.3 T. Below room temperature down to 4.5 K a Lake Shore ac susceptometer ($\mu_o H_{ac}$ = 1 mT, f = 133.3 Hz) was applied, quoting both the real and the imaginary parts of the dynamic susceptibility. Magnetization versus temperature (5 K < T < 300 K) in external field B = 0.1 T as well as isothermal (T = 5 K) magnetization versus field (B = 0–3 T) were recorded employing a SHE-SQUID magnetometer.

Electronic band structure calculations. Extended Hückel tight-binding (6) calculations were carried out on the crystal structure of $Sm_5B_2C_5$ using the program YAeHMOP (7). The exponents (ζ) and the valence shell ionization potentials (H_{ii} in eV) were, respectively, 1.3, −15.2 for B 2s; 1.3, −8.5 for B 2p; 1.625, −21.4 for C 2s; 1.625, −11.4 for C 2p; 2.14, −7.24 for Sm 6s; and 2.08, −4.65 for Sm 6p. The H_{ii} value for Sm 5d was −8.08. A linear combination of two Slater-type orbitals with exponents ζ_1 = 3.78 and ζ_2 = 1.381 with the weighting coefficients c_1 = 0.7765 and c_2 = 0.4586 were used to represent the Sm 5d atomic orbitals.

Self-consistent *ab initio* band structure calculations were performed on the crystal stuctures of $Sm_5B_2C_5$ and

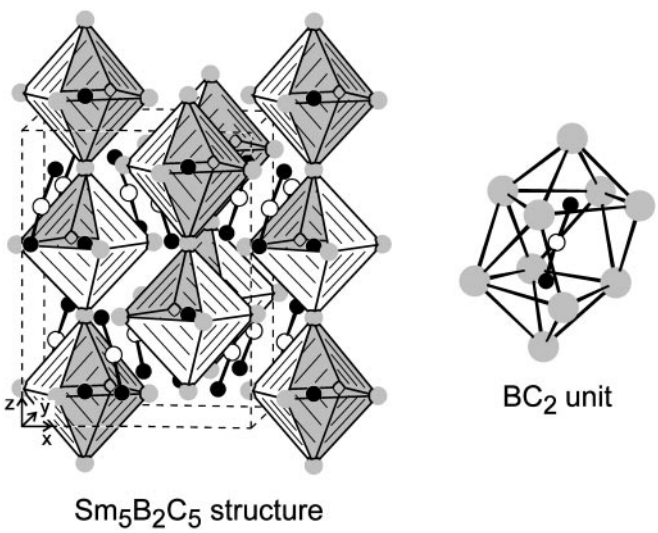

FIG. 1. Crystal structure of $Sm_5B_2C_5$ (left). The chains of edge-sharing Sc_6C octahedra and the BC_2 units are emphasized. The distorted square antiprismatic coordination of the BC_2 unit is shown on the right. Gray, white, and black balls represent Sm, B, and C atoms, respectively.

$Gd_5B_2C_5$ with the scalar relativistic tight binding linear muffin-tin orbital method in the atomic sphere approximation (LMTO-ASA) including the combined correction (8). Exchange and correlation were treated in the local density approximation using the von Barth-Hedin local exchange correlation potential (9). The Wigner-Seitz's atomic sphere radii were determined using the automatic procedure (10). Interatomic spaces were filled with interstitial spheres. The full LMTO basis set consisted of 6*s*, 6*p*, 5*d*, and 4*f* functions for Sm and Gd spheres, 2*s*, 2*p*, and 3*d* functions for B and C spheres, and *s*, *p*, and *d* functions for "empty spheres." The eigenvalue problem was solved using the following minimal basis set obtained from Löwdin downfolding technique (11): Gd and Sm 4*f*, 5*d*, and 6*s*, B and C 2*s* and 2*p*, and interstitial *s* LMTOs. The *k* space integration was performed using the tetrahedron method (12). Charge self-consistency and average properties were obtained from 6 irreducible *k* points.

DESCRIPTION OF THE STRUCTURE

The crystal structure of the $R_5B_2C_5$ compounds is closely related to the crystal structure of $R_5B_2C_6$ (R = La (13), Ce (14)). The metallic sublattice consists of a three-dimensional framework resulting from the stacking of slightly corrugated two-dimensional square nets rotated by about 45° from each other. Such a stacking along the *c* direction leads to the formation of octahedral holes and distorted bicapped square antiprismatic cavities in which are trapped isolated carbon atoms and C–B–C chains respectively (see Fig. 1 for $Sm_5B_2C_5$). These chains are nearly linear with B–C distances of 1.47(2) and 1.46(1) Å in $Sm_5B_2C_5$ and $Gd_5B_2C_5$, respectively, suggesting double bond character. Indeed, each carbon atom of the BC_2 groups is accomodated in an $[R_5B]$ octahedron, a common feature in the ternary rare-earth metal boron carbide compounds (1). The presence of only one carbon atom in the nearly regular rare-earth metal octahedra in $R_5B_2C_5$ instead of a C_2 dumbbell as observed in $R_5B_2C_6$ is probably due to the smaller size of the rare-earth metal in play (it is noteworthy to mention that both stoichiometries $R_5B_2C_5$ (with isolated C atoms) and $R_5B_2C_6$ (with C_2 units) exist only for Ce). Nevertheless, we should point out that elongated rare-earth metal octahedra with C_2 pairs occur in the whole series of binary RC_2 carbides. *R*–*R*, *R*–B(1), *R*–C(1), and *R*-C(2) bonding contacts (which are in the range of 3.48–3.83, 2.68–2.82, 2.50–2.74 and 2.53–2.81 Å for $Sm_5B_2C_5$ for instance) are comparable to those commonly measured in this kind of compound (1). A detailed description of the $Sm_5B_2C_5$ structure together with the related structures of $Ce_5B_2C_6$ (14) and binary Sc_3C_4 (5) will be published in a forthcoming paper devoted to the twinning in these structures (15).

ELECTRONIC STRUCTURE

Initially observed in $R_5B_2C_6$ (R = La (13), Ce (14)) and Sc_2BC_2 (16), tightly bonded BC_2 groups are now frequently encountered in solid-state chemistry (17–26). Previous theoretical studies on Sc_2BC_2 for instance (16) have shown that a formal charge of 5- is energetically most favorable for an isolated linear or nearly linear BC_2 unit, since it provides a large HOMO/LUMO gap separating the low-lying bonding and nonbonding levels from the high-lying antibonding levels. Such a charge assignment, which accounts for the B–C double bond character generally observed and renders it isoelectronic to CO_2 (16), leads to the formal charge distribution $(R^{3+})_5(BC_2^{5-})_2(C^{4-})(e^-)$ for the title compounds. With one electron per unit delocalized in metallic states, a poor metallic behavior is expected as confirmed experimentally and theoretically (see below). However, such a salt-like charge assignment discards the strong covalent bonding, which may occur between the metal and nonmetal atoms.

Extended Hückel tight-binding (EHTB) calculations were first carried out on $Sm_5B_2C_5$ in order to provide a qualitative orbital analysis of the bonding of the isolated carbon atoms and the BC_2 groups within the metallic matrix in the title compounds. The computed density of states (DOS) shown in Fig. 2 reveals a strong resemblance to the one computed previously for Sc_2BC_2 (16). The DOS separates broadly into two parts. The lowest part, extending over the energy range −11 to −15 eV, derives predominantly from the boron and carbon orbitals, whereas the highest part, which extends above −10 eV, is made up mainly from the metal orbitals. Decomposition of the contributions to this DOS of the different constituting groups, illustrated in Fig. 2, indicates a rather strong covalent character between the metallic matrix and the BC_2 and C "ligands" with the presence of a metallic participation in the boron–carbon

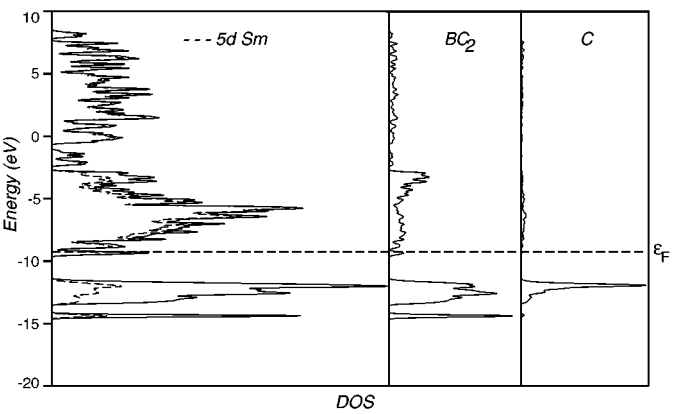

FIG. 2. EHTB DOS of $Sm_5B_2C_5$: (a) total (solid line) and Sm atomic contribution (dashed line), (b) BC_2 contribution, and (c) "isolated" carbon atomic contribution.

valence "band," and vice versa some participation of the BC_2 groups and C atoms in the conduction "band." These strong covalent interactions lead to significant electron transfer between the interacting "ions," as exemplified by the computed net charges:

$$(Sm^{1.46+})_5\ [(BC_2)^{2.59-}]_2\ C^{2.14-}.$$

As illustrated in Fig. 3 and Table 1, this electron transfer results primarily from electron donation from the occupied bonding and nonbonding frontier orbitals (FO) of the $(BC_2)^{5-}$ groups (and C^{4-} atoms) into empty metallic states (see the small peaks of projected DOS above the Fermi level in the metallic band in Fig. 3). This electron donation (3.60 electrons) is more important than the corresponding donation (2.52 electrons) computed for Sc_2BC_2 (compare the FO occupations of BC_2 in Table 1) (16). On the other hand, with formally only one electron per Gd_5 backdonation from the metal atoms toward acceptor π^* orbitals of the the $(BC_2)^{5-}$ units is much weaker than that computed for Sc_2BC_2 (0.05 vs 0.23 electron) (16). More donation from the BC_2 chains toward the metal atoms (which weakens the B–C bonding) and less backdonation from the metals into BC_2 acceptor orbitals (which strengthen the B–C bonding) with respect to Sc_2BC_2 leads to comparable B–C overlap population in $Sm_5B_2C_5$ and Sc_2BC_2 (1.16 vs 1.11). This reflects in the close B–C separations measured experimentally (1.467 vs 1.484 Å).

One of the main limitations of these EHTB computations is that they do not consider explicitly the *R* 4*f* orbitals. Although it is generally accepted that they play a minor role in the metal–nonmetal bonding (1) their absence prevents us from presenting a fully reliable electronic structure and from interpreting the magnetic properties of the title compounds. Thus, spin-polarized LMTO calculations were performed on $Gd_5B_2C_5$ to complement EHTB calculations. The resulting total and projected spin-polarized densities of states are separately depicted in Figs. 4 and 5, showing the spin-up and spin-down states. Examination of these DOS indicate that the spin-up and spin-down 4*f* states are separated by ca. 4.5 eV, a value which might be underestimated but commonly computed with the LMTO method for Gd-containing compounds (27). Both spin-up and spin-down 4*f* manifolds are rather spread out over ca. 1.5 eV, reflecting some mixing with Gd 5*d* orbitals as well as with BC_2 and C orbitals. The conduction band is preferentially made up from the metal 5*d* states, whereas the valence band derives mainly from BC_2 and C states. Nevertheless, as noted above for the qualitative EHTB results on $Sm_5B_2C_5$, some presence of a metallic participation in the valence band and

TABLE 1
Some EHTB Characteristics Computed for Sc_2BC_2 (16) and $Sm_5B_2C_5$

Compound	Sc_2BC_2	$Sm_5B_2C_5$
Fermi level (eV)	−9.506	−9.344
	Overlap population (distance)	
B–C	1.107 (1.467 Å)	1.156 (1.482 Å)
	Atomic net charges	
R	1.24	1.46
B	0.55	0.579
C (BC_2)	−1.51	−1.587
C	—	−2.14
	BC_2 FO occupations	
σ_g^+	1.598	1.376
π_u	3.269	2.901
σ_u^+	1.630	1.493
π_g	2.981	2.627
π_u^*	0.229	0.046

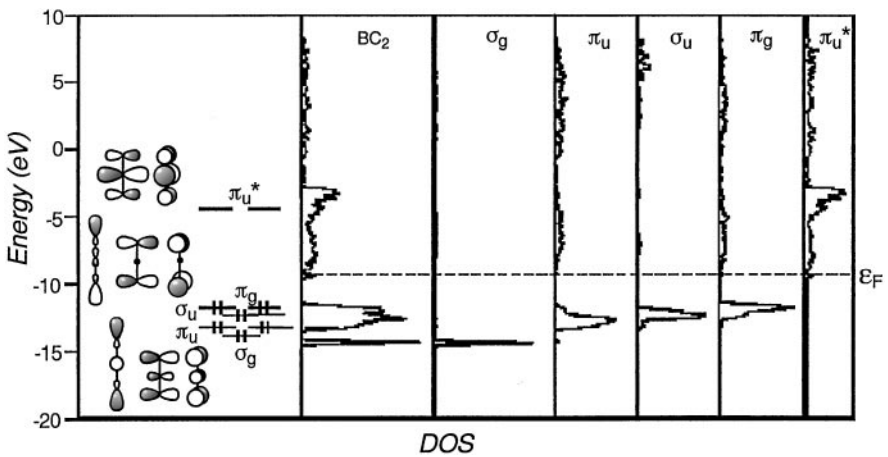

FIG. 3. BC_2 FO contributions to the EHTB DOS of $Sm_5B_2C_5$. The EH molecular orbital diagram of an isolated BC_2 unit is recalled on the left.

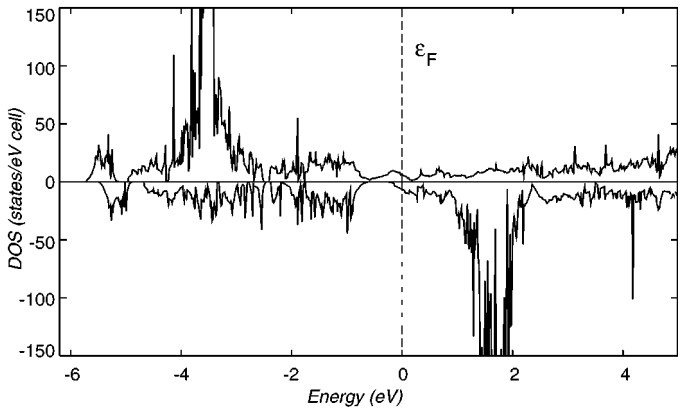

FIG. 4. Total spin-up and spin-down LMTO DOS for $Gd_5B_2C_5$.

some participation of the BC_2 groups and C atoms in the conduction band are confirmed (28). This establishes clearly that strong covalent interactions occur between the metallic matrix and the BC_2 and C "ligands" in this kind of compound.

Spin-up and spin-down Gd 5*d* states are separated by ca. 0.5 eV around the Fermi level. This slight polarization of the conduction band indicates that $Gd_5B_2C_5$ is a magnetic metal and leads to a weak enhancement of the number of unpaired electrons per Gd center (7.1 instead of 7 expected for a half-filled 4*f* band). The BC_2 projected DOS is also slightly affected by the spin polarization around the Fermi level, whereas the C projected DOS is unaffected (see Fig. 5).

Spin-polarized LMTO calculations, performed on $Sm_5B_2C_5$ provided a DOS with a shape highly comparable to that computed for $Gd_5B_2C_5$. Here again, the slight polarization of the 5*d* conduction electrons slightly increases the number of magnetic electrons (an excess of 0.4 with respect to the expected value of 5).

MAGNETIC PROPERTIES

The magnetic behavior of the ternary compounds $R_5B_2C_5$ (R = Ce–Sm, Gd–Tm) is generally characterized by the onset of ferromagnetic order of the rare-earth sublattice. The results are summarized in Figs. 6–12 and Table 2. In the paramagnetic regime, $T_C < T \leq 500$ K, the susceptibility data of the Gd–Tm-containing samples (the ceric compounds were not single-phase) follow a Curie–Weiss law (see Fig. 6). The magnetic constants, the effective moment μ_{eff} and the paramagnetic Curie temperature θ_p, were calculated by a least-squares fit according to the equation

$$\chi = \frac{C}{T - \theta_P} + \chi_o. \qquad [1]$$

The values for the effective moments are in good agreement with the theoretical moments of the tripositive rare-earth metals (see Table 2). The values of $\chi_o = \chi_{Pauli} - \chi_{Dia} - \chi_{Landau}$, being small, were consequently neglected. All samples (including the ceric borocarbides) exhibit ferromagnetic ordering (confirmed by the temperature dependence of the imaginary part of χ_{AC}) upon lowering the temperature, which is in accord with the observed positive values Θ_p. The measured ordering temperatures, $\chi^{max} = T_C$, increase in case of the Ce–Sm-containing samples, whereas they decrease for the heavy rare-earth metal borocarbides

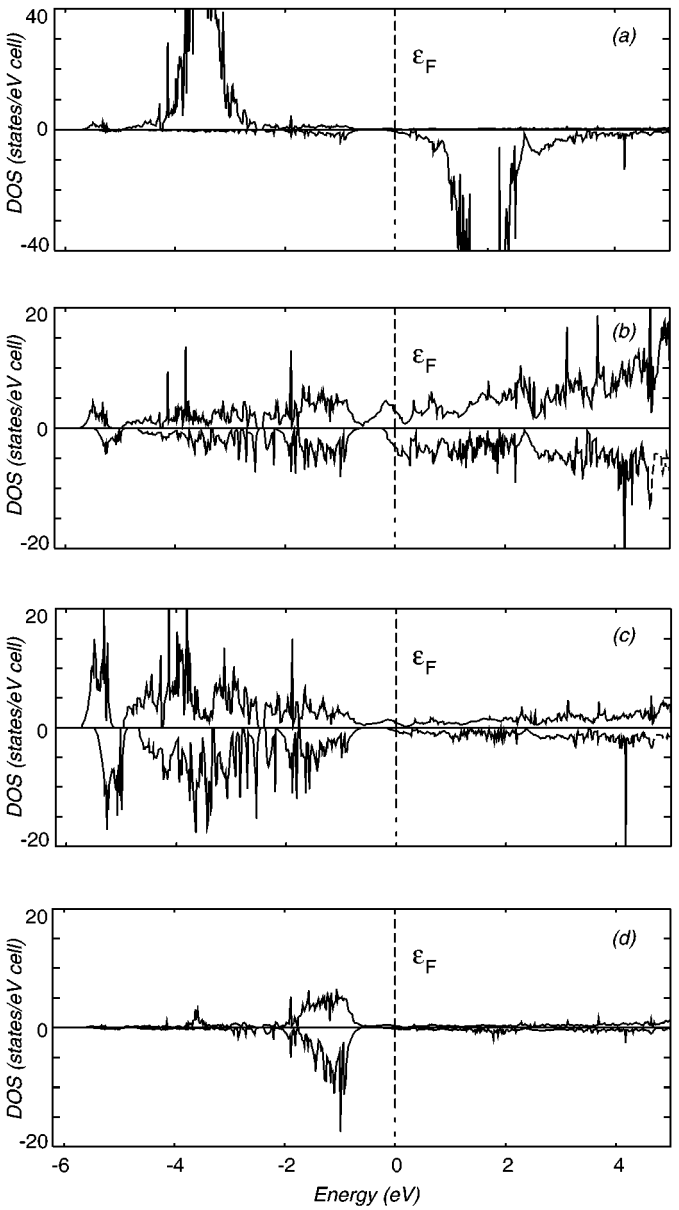

FIG. 5. Projected spin-up and spin-down LMTO DOS for $Gd_5B_2C_5$: (a) Gd *f* orbitals, (b) Gd *d* orbitals, (c) BC_2 units, and (d) C atoms.

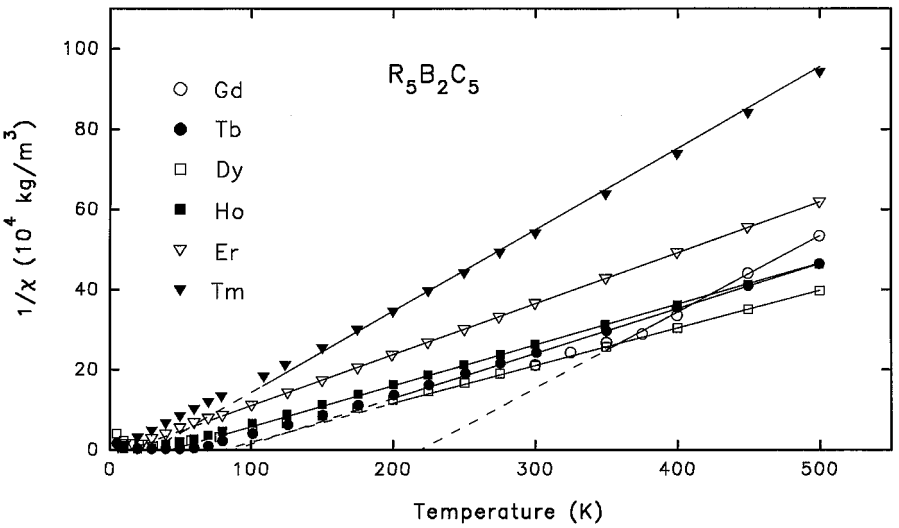

FIG. 6. Reciprocal susceptibilities versus temperature for compounds $R_5B_2C_5$; solid lines calculated using Eq. [1].

upon increasing of the R atomic number (see Table 2). T_C as well as Θ_p values approximately scale with the de Gennes factor, indicating that the coupling of the R–R moments is due to the indirect exchange interaction via the conduction electrons (RKKY interaction). Note that no further analysis was done for the cerium-, praseodymium-, neodymium-, and samarium-containing samples which could not be obtained as single phase. The secondary phase is in any case the structurally related $R_5B_2C_6$ compound, exhibiting in general lower ordering temperatures than the $R_5B_2C_5$ series and will be reported in a forthcoming paper.

The compound $Gd_5B_2C_5$ shows a rather peculiar magnetic behavior when compared with the related antiferromagnetic compound $Gd_5B_2C_6$ (3). The magnetization of a zero field cooled (zfc) sample increases in a moderate external field, passes a broad maximum, and decreases sharply at the Curie temperature. When the sample is measured under the same conditions, but after having been fully magnetized (fm, $B = 3$ T), the higher "frozen-in" net magnetization first decreases as the temperature increases, passes a minimum, and merges into the zfc curve above ca. 50 K (see Fig. 7). The isothermal magnetization versus field at $T = 5$ K reveals a remarkable hysteresis loop between increasing and decreasing fields (see Fig. 7, inset). Broad maxima in the $M(T)$ curves are usually observed in systems exhibiting narrow-domain-wall ferromagnetism together with large magnetocrystalline anisotropy effects (see below) or in compounds developing micromagnetism. Since in the

TABLE 2
Crystallographic and Magnetic Data measured for the Ternary Compounds $R_5B_2C_5$ (R = Y, Ce–Tm), (space group $P4/ncc$–D^8_{4h}, No. 130)

Compound	Lattice Parameters (nm, nm^3) a	c	V	T_C (K)	θ_p (K)	μ_{eff} (μ_B)	μ_S (μ_B)	Remanence (%)	Critical field (T)
$Ce_5B_2C_5$	0.85708(5)	1.1004(1)	0.8083(1)	7	—	—	—	—	—
$Pr_5B_2C_5$	0.8522(1)	1.0995(2)	0.7985(3)	20	—	—	—	—	—
$Nd_5B_2C_5$	0.84872(5)	1.09591(8)	0.7894(1)	45	—	—	—	—	—
$Sm_5B_2C_5$	0.8331(1)	1.0926(7)	0.7583(5)	22	no CW	—	—	—	—
$Gd_5B_2C_5$	0.82455(3)	1.08550(6)	0.73801(7)	130	219.5	7.6	6.8	—	—
$Tb_5B_2C_5$	0.81382(6)	1.0861(3)	0.7194(2)	42	87.5	9.8	5.4	36	0.2
$Dy_5B_2C_5$	0.80869(2)	1.0838(3)	0.7088(2)	30	72.2	11.0	5.7	18	0.1
$Ho_5B_2C_5$	0.80355(8)	1.0827(1)	0.6991(2)	21	43.8	10.6	6.3	12	0.1
$Er_5B_2C_5$	0.79892(9)	1.0740(2)	0.6855(2)	22	13.5	9.6	5.3	6	0.05
$Tm_5B_2C_5$	0.79299(4)	1.0810(1)	0.6798(1)	4.5	29.5	7.7	6.3	—	—
$Y_5B_2C_5$	0.81069(9)	1.0824(3)	0.7114(3)	paramagnetic, $T < 300$ K, $\chi \leq 2.3 \times 10^{-7}$ m^3/kg					

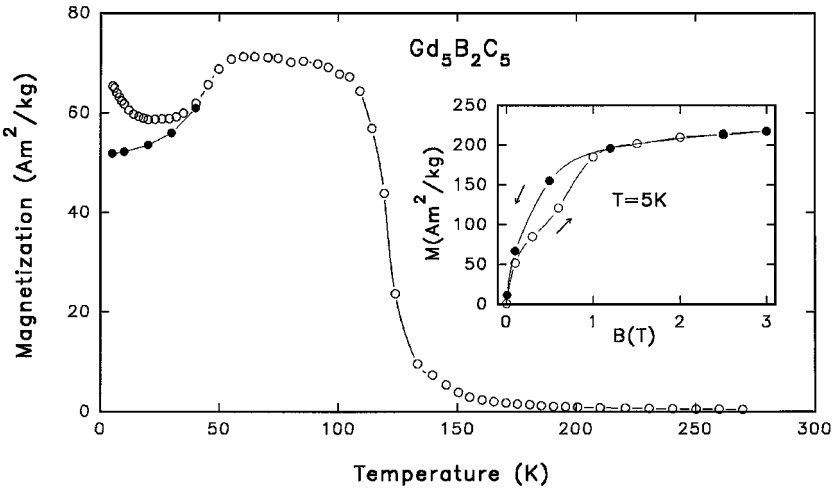

FIG. 7. Magnetization vs temperature for $Gd_5B_2C_5$ in external field 0.1 T. Filled circles, zfc sample; open circles, fm sample. (Inset) Magnetization vs field at 5 K.

case of Gd, where $L = 0$, anisotropy must be excluded, we suggest the following: the magnetic ground state of $Gd_5B_2C_5$ resembles a "spin glass"-like (asperomagnetism) or "cluster glass"-like state (micromagnetism) (29). In an external field higher than 0.5 T a spin reorientation takes place, leading to an almost colinear spin arrangement above 1 T. The derived saturation moment $\mu_S = 6.8\ \mu_B \sim$ gJ is in good accordance with this assumption. The difference of the $M(T)$ curves measured in increasing temperature and in moderate external fields (see Fig. 7) strongly depends on experimental history (zfc or fm sample) and is attributed to the spin-glass freezing below $T_{SG} \sim 55$ K associated with the thermal blocking of clusters' moments.

The temperature dependence of the magnetization curves of the Tb–Tm borocarbides in the ordered state is reminiscent of the typical behavior of narrow-domain-wall

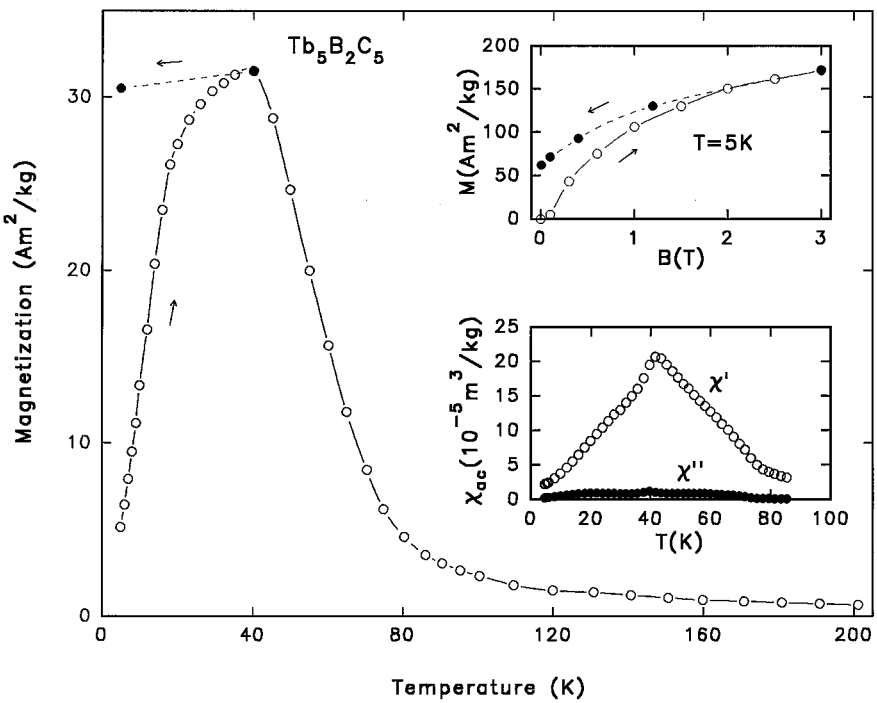

FIG. 8. Magnetization vs temperature for $Tb_5B_2C_5$ in external field 0.1 T. Open circles, zfc sample; filled circles, fc sample. (Top inset) Magnetization vs field at 5 K. (Bottom inset) Dynamic susceptibilities vs temperature.

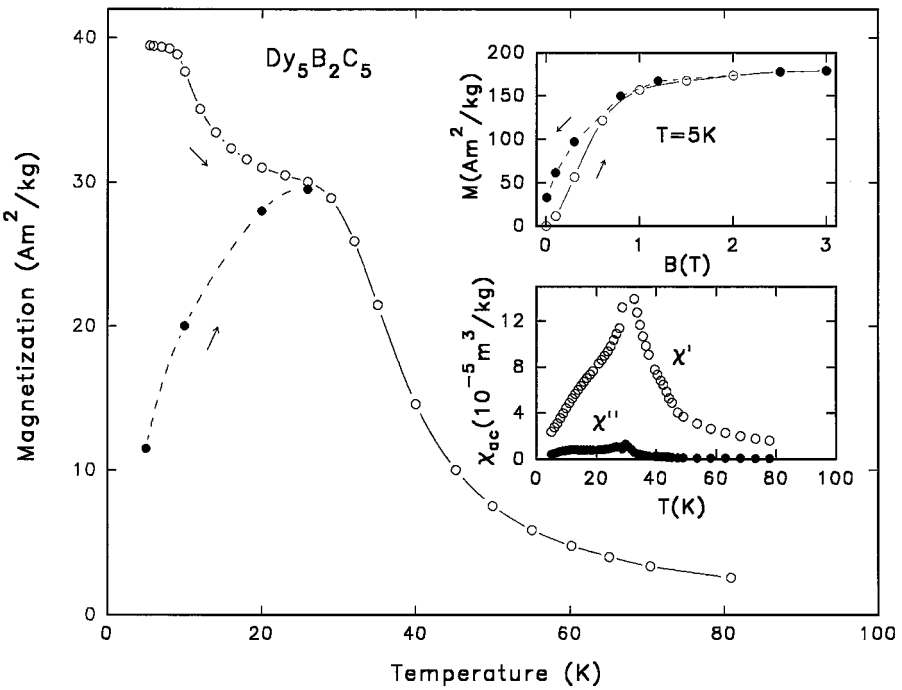

FIG. 9. Magnetization vs temperature for $Dy_5B_2C_5$ in external field 0.1 T. Filled circles, zfc sample; open circles, fm sample. (Top inset) Magnetization vs field at 5 K. (Bottom inset) Dynamic susceptibilities vs temperature.

ferromagnets (30), where wall movement is thermally activated in applied fields (see Figs. 8–12). The critical field, B_{crit}, where wall propagation sets in, is close to the coercive field, B_{coerc} and was estimated from isothermal magnetization plots at $T = 5$ K ($B_{crit} \sim B_{coerc}$; see Figs. 8–12, insets). These data, listed in Table 2 together with the values for the

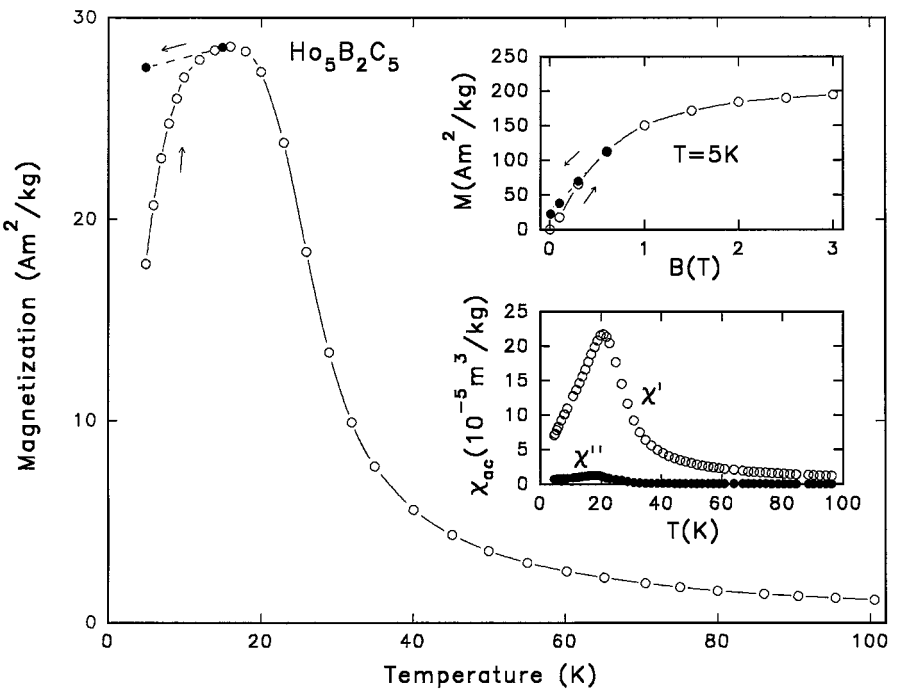

FIG. 10. Magnetization vs temperature for $Ho_5B_2C_5$ in external field 0.1 T. Open circles, zfc sample; filled circles, fc sample. (Top inset) Magnetization vs field at 5 K. (Bottom inset) Dynamic susceptibilities vs temperature.

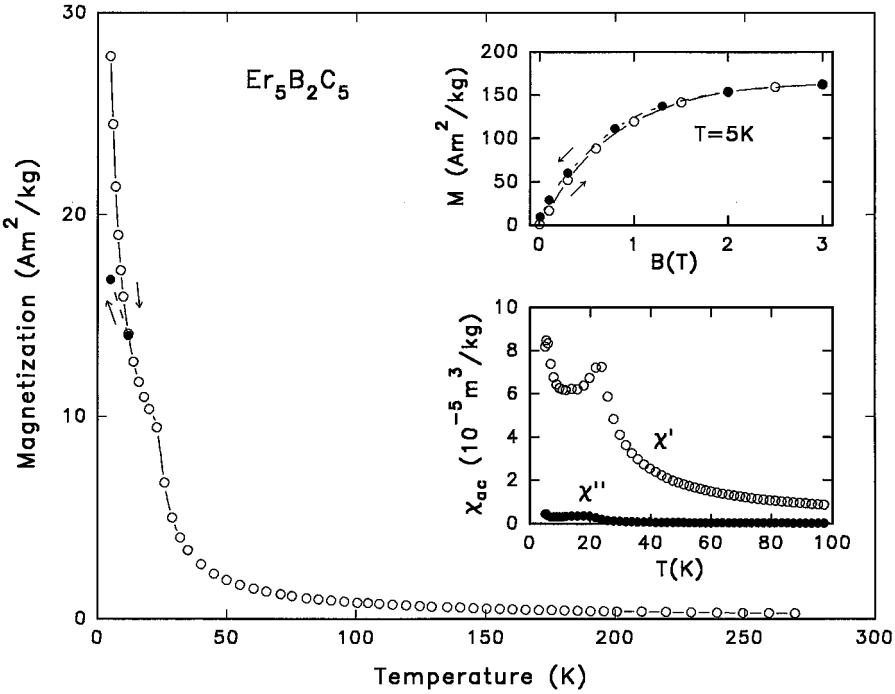

FIG. 11. Magnetization vs temperature for $Er_5B_2C_5$ in external field 0.1 T. Open circles, fm sample, filled circles, fc sample. (Top inset) Magnetization vs field at 5 K. (Bottom inset) Dynamic susceptibilities vs temperature.

remanent magnetization M_R (in percentage of the saturation magnetization at $B = 3$ T and $T = 5$ K) are maximal in the case of $Tb_5B_2C_5$ ($B_{crit} \sim 0.2$ T; $M_R \sim 36\%$) (Table 2) and decrease as the atomic number of the rare-earth metals increases. The presence of narrow domain walls can be understood as the result of a high magnetocrystalline

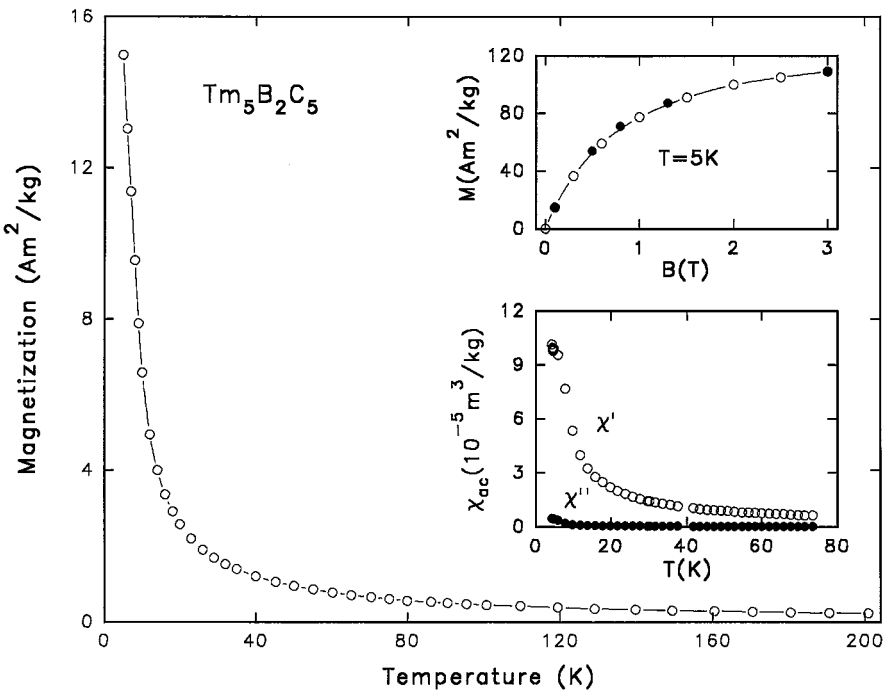

FIG. 12. Magnetization vs temperature for $Tm_5B_2C_5$ in external field 0.1 T. (Top inset) Magnetization vs field at 5 K. (Bottom inset) Dynamic susceptibilities vs temperature.

anisotropy energy caused by the crystal field interaction of the moments containing an orbital contribution. Finally the values of the saturation moments are close to one half of the expected value gJ (see Table 2), which is a good indication for polycrystalline samples (randomly oriented fixed powder) that the vector of magnetization coincides rather with the crystallographic *c*-axis (easy-axis anisotropy). The Tm-containing compound, however, seems to favor easy-plane anisotropy.

ACKNOWLEDGMENTS

We thank Prof. Dr. h.c. mult. A. Simon (MPI-FKF Stuttgart) for the use of the image plate diffractometer. K.H., J.B., and J.-F.H. are grateful to the Österreichischer Akademischer Austauschdienst (Austria) and the Ministère des Affaires Etrangères (France) for travel grants (Amadeus program) which have greatly facilitated these studies. We are grateful to Prof. O. K. Andersen and Dr. O. Jepsen (Max-Planck-Institut für Festkörperforschung, Stuttgart) for making the LMTO program available to us and for their helpful comments.

REFERENCES

1. J. Bauer, J.-F. Halet, and J. Y. Saillard, *Coord. Chem. Rev.* **178–180,** 723 (1998) and references therein.
2. G.-Y. Adachi, N. Imakana, and Z. Fuzhong, *in* "Handbook on the Physics and Chemistry of Rare Earths" (K. A. Gschneidner, Jr., and L. Eyring, Eds.), Vol. 15, p. 62. Elsevier, Amsterdam, 1991.
3. E. Bidaud, K. Hiebl, J. Bauer, and P. Rogl, *J. Alloys Compd.* **266,** 1 (1998).
4. E. Bidaud, K. Hiebl, and J. Bauer, *J. Alloys Compds.* **279,** 97 (1998).
5. R. Pöttgen and W. Jeitschko, *Inorg. Chem.* **30,** 427 (1991).
6. (a) R. Hoffmann, *J. Chem. Phys.* **39,** 1397 (1963); (b) M.-H. Whangbo and R. Hoffmann, *J. Am. Chem. Soc.* **100,** 6093 (1978).
7. G. A. Landrum, "YAeHMOP — Yet Another Extended Hückel Molecular Orbital Package," release 2.0: Ithaca, NY, 1997.
8. (a) O. K. Andersen, *Phys. Rev. B* **12,** 3060 (1975); (b) O. K. Andersen, *Europhys. News* **12,** 4 (1981); (c) O. K. Andersen, *in* "The Electronic Structure Of Complex Systems" (P. Phariseau and W. M. Temmerman, Eds.). Plenum, New York **(**1984); (d) O. K. Andersen and O. Jepsen, *Phys. Rev. Lett.* **53,** 2571 (1984); (e) O. K. Andersen, O. Jepsen, and M. Sob, *in* "Electronic Band Structure and Its Application" (M. Yussouf, Ed.). Springer-Verlag, Berlin, 1986; (f) H. L. Skriver, "The LMTO Method." Springer-Verlag, Berlin, 1984.
9. U. von Barth and L. Hedin, *J. Phys. C* **5**, 1629 (1972).
10. O. Jepsen and O. K. Andersen, *Z. Phys. B* **97**, 35 (1995).
11. W. R. Lambrecht and O. K. Andersen, *Phys. Rev. B* **34,** 2439 (1986).
12. P. E. Blöchl, O. Jepsen, and O. K. Andersen, *Phys. Rev. B* **49,** 16223 (1994).
13. J. Bauer and O. Bars, *J. Less-Common Met.* **95,** 267 (1983).
14. J. Bauer and O. Bars, *J. Less-Common Met.* **83,** 17 (1983).
15. R.-D. Hoffmann, R. Pöttgen, J. Bauer, and J.-F. Halet, unpublished results.
16. J.-F. Halet, J.-Y. Saillard, and J. Bauer, *J. Less-Common Met.* **158,** 239 (1990).
17. Hj. Mattausch and A. Simon, *Angew. Chem. Int. Ed. Engl.* **34,** 1633 (1995).
18. Hj. Mattausch, A. Simon, C. Felser, and R. Dronskowski, *Angew. Chem. Int. Ed. Engl.* **35,** 1685 (1996).
19. D. Ansel, J. Bauer, F. Bonhomme, G. Boucekkine, G. Frapper, P. Gougeon, J.-F. Halet, J. Y. Saillard, and B. Zouchoune, *Angew. Chem. Int. Ed. Engl.* **35,** 2098 (1996).
20. H. Hillebrecht and F. D. Meyer, *Angew. Chem. Int. Ed. Engl.* **35,** 2499 (1996).
21. O. Reckeweg and H.-J. Meyer, *Angew. Chem. Int. Ed. Engl.* **37,** 3407 (1998).
22. O. Oeckler, V. Duppel, Hj. Mattausch, and A. Simon, *Inorg. Chem.* **38,** 1767 (1999).
23. Hj. Mattausch, O. Oeckler, and A. Simon, *Inorg. Chim. Acta* **289,** 174 (1999).
24. Y. Shi, A. Leithe-Jasper, and T. Tanaka, *J. Solid State Chem.* **148,** 250 (1999).
25. Y. Shi, L. Bourgeois, A. Leithe-Jasper, Y. Bando, and T. Tanaka, *J. Alloys Compds.* **298,** 99 (2000).
26. C. Jardin, O. Oeckler, Hj. Mattausch, A. Simon, J.-F. Halet, J.-Y. Saillard, and J. Bauer, *Inorg. Chem.*, in press.
27. See for example C. Felser, K. Ahn, R. K. Kremer, R. Seshadri, and A. Simon, *J. Solid State Chem.* **147,** 19 (1999).
28. As often observed in this kind of compound, an energy gap is computed between the valence and conduction band within EHTB calculations. The corresponding energy gap generally vanishes within density functional calculations (see Ref. 26 for instance).
29. C.M. Hurd, *Contemp. Phys.* **23**(5), 469 (1982).
30. B. Barbara, C. Bècle, R. Lemaire, and D. Paccard, *J. Phys.* **32,** C1 (1971).